Acta Materialia 289 (2025) 120857

Contents lists available at ScienceDirect

Acta Materialia

journal homepage: www.elsevier.com/locate/actamat

Full length article

Metastable AlB_2 structured TM-Si-$B_{2\pm z}$ (TM = Ti, Zr, Hf) solid solutions from first-principles

C. Gutschka [a,c,*], L. Zauner [a], T. Glechner [a], D. Holec [b], H. Riedl [a,c]

[a] Christian Doppler Laboratory for Surface Engineering of high-performance Components, TU Wien, 1060, Vienna, Austria
[b] Department of Materials Science, Montanuniversität Leoben, 8700, Leoben, Austria
[c] Institute of Materials Science and Technology, TU Wien, 1060, Vienna, Austria

ARTICLE INFO

Keywords:
Borides
DFT
Si alloying
Ternary diborides
Phase stabilities

ABSTRACT

AlB_2 structured transition metal diborides are a class of refractory ceramics standing out through their high-temperature stability and exceptional mechanical properties, encouraging research on their bulk and thin film forms. In Physical Vapor Deposition (PVD), scientific interest has focused on growing metastable solid solutions with Si to enhance oxidative properties and fracture characteristics. However, theoretical investigations of such ternary compounds are still rare. Therefore, this study explores the structural, energetical, and mechanical properties of the Ti-Si-B_2, Zr-Si-B_2, and Hf-Si-B_2 structures, as well as their vacancy dynamics, with the help of Density Functional Theory (DFT). For all three systems, silicon prefers the boron sublattice and via structural analysis, metastable solubility limits of 24 at. %, 27 at. %, and 25 at. % of Si in $Ti(Si,B)_2$, $Zr(Si,B)_2$, and $Hf(Si,B)_2$, could be established, respectively. An analysis of simulated XRD patterns, Radial Distribution Functions (RDFs), and Crystal Orbital Hamilton Populations (COHPs), attributed an observed destabilization of the AlB_2-type symmetry to Si clustering. Simulated elastic properties revealed a decrease of the Young's moduli with increasing silicon contents, reproducing experimental values up to 15 at. % Si. The study discovered a structural instability of ternary, metastable AlB_2-type compounds concerning metal vacancies.

1. Introduction

Transition metal diborides (TMBs) stand out with extraordinary mechanical properties (i.e. superhardness), combined with high melting temperatures and thermal stability [1–3]. In several experimental studies transition metal diboride-based bulk materials and thin films – the latter are typically synthesized via the method of Physical Vapor Deposition (PVD) – have been proven to be stabilized in the AlB_2 structure type, also known as the α-type [4], being part of the Space Group (SG) 191 ($P6/mmm$). These compounds are known to show strong sp^2-sp^3 hybridization of the boron orbitals, while the directional B-B bonds form hexagonal sheets within the basal plane. Mixed covalent-ionic TM-B interactions are less strong, but give rise to minor ductility, whereas mainly metallic TM-TM bonds are of negligible contribution to the cohesive energy, but lead to moderate electrical conductivity [3,5–7]. Apart from that, the excellent mechanical properties of α-structured diborides grown by plasma assisted techniques (PVD) also rely on their intrinsic anisotropic character and a twofold-morphology. This morphology typically consists of 001-oriented, columnar nanometer-sized grains surrounded by an amorphous, boron rich tissue phase [3,8–10]. This tissue phase is also a key feature for their fracture resistance as shown for $TiB_{2\pm z}$ [11]. However, for diboride-based materials and in particular thin films, their low oxidation resistance and brittle nature still limit competitiveness with established oxide- and nitride-based thin film ceramics [3,12–15]. In contrast to bulk diboride ceramics, where established two phased materials such as TMBs/SiC are typically used in extremely oxidative environments [16,17], in thin film research ternary, quaternary, and even compositionally more complex compounds (i.e. high entropy borides) are suggested to overcome these limitations [18–31]. This discrepancy mainly stems from the extreme synthesis conditions encountered in PVD, allowing to quench-in highly defected, metastable structures [32–35], while bulk ceramics usually are near-equilibrium after fabrication. For example, alloying of strong oxide formers such as X=Si, Al, or Cr has shown promising results for metatstable PVD thin film materials, with several studies verifying the existence of single phased, AlB_2 structured TM-X-$B_{2\pm z}$ solid solutions up to specific alloy contents [20,26,29,36–40]. Compared to Al and Cr, Si showed by far the best oxidation resistance and acceptable hardness values at temperatures around 1200 °C [41,42].

* Correspondence to: Christian Doppler Laboratory for Surface Engineering of high-performance Components, TU Wien, Getreidemarkt 9/E308-01-02, A-1060, Vienna, Austria.
E-mail address: christian.gutschka@tuwien.ac.at (C. Gutschka).

https://doi.org/10.1016/j.actamat.2025.120857
Received 17 October 2024; Received in revised form 19 February 2025; Accepted 20 February 2025
Available online 4 March 2025
1359-6454/© 2025 The Authors. Published by Elsevier Inc. on behalf of Acta Materialia Inc. This is an open access article under the CC BY license (http://creativecommons.org/licenses/by/4.0/).

Furthermore, quaternary extensions of Si containing alloy concepts have lead to even further improvements [30,31]. However, the existence of TM-Si-$B_{2\pm z}$ solid solutions appears to challenge conventional equilibrium thermodynamics.

Multiple experimental studies have reported decent solubility of diborides MB_2 (M = Ti, V, Zr, Nb, Hf, Ta, W, Al) within each other and were readily supported by theoretical investigations [43–47], leading to the currently prominent research area of mixed metal diborides $M^1{}_{1-x}M^2{}_xB_2$ and their high entropy extension [48–52]. Focusing on thin film applications, H. Euchner et al. [53] and B. Alling et al. [54] investigated $M^1{}_{1-x}M^2{}_xB_2$'s with ab initio methods, reporting structural distortion and miscibility gaps, discovering a potential for age hardening. However, evaluations of TM-Si-B phase diagrams (TM = Ti, V, Zr, Nb, Hf, Mo, Cr) all found negligible solubilities of Si in equilibrium AlB_2-type borides [55–63], whereas other boride phases, such as NbB and Nb_3B_4, persisted low finite Si intake of 4 at. % and 3 at. %, respectively [64,65]. Similar to boride phases, most transition metal silicides showed negligible solubility for B — just Cr_5Si_3 exhibited a maximal intake of 4 at. % B [64–68] — but mixed metal disilicides $M^1{}_{1-x}M^2{}_xSi_2$ were readily encountered [69–72].

Even though above insights manifest the improbable incorporation of Si into AlB_2-type transition metal diborides, thin films of TM-Si-$B_{2\pm z}$ are typically classified as α-structured solid solutions, verified by different diffraction techniques such as XRD or SAED in several studies [30,31,40–42]. While their metastable appearance is experimentally proven for TM-Si-$B_{2\pm z}$ thin film materials, limited knowledge has been gathered in terms of theoretical understanding. For example, T. Glechner et al. [42] suggested nano-sized, Si rich clusters within the grains of Hf-Si-$B_{2\pm z}$ for Si contents around 20 at. %. However, L. Zauner et al. [40] used Atom Probe Tomography (APT) to investigate the exact distribution of Si in Cr-Si-$B_{2\pm z}$ thin films, reporting an inhomogeneous Si distribution and segregation at grain boundary phases. Since equilibrium phase diagrams would suggest decomposition, the maximal alloy content dissolvable in a metastable single phased AlB_2 structured thin film remains unclear [36–40,42]. In order to predict metastable solubility limits, diverse ab initio-based studies focused on near-equilibrium thermodynamic descriptors, such as energies of formation E_f and enthalpies of mixing, with varying performance [46,47,53,73–75]. Conversely, prioritizing low structural distortion in compounds while solely requiring their negative E_f has also matched DFT-simulated metastable solubility limits with Cr-Si-$B_{2\pm z}$ thin films [40]. Tracking the structural integrity of metastable solid solutions thus appears as the major ingredient for locating solubility limits, with E_f depicting a guideline for lattice occupations.

Therefore, in this study, DFT was used to obtain insights into the fundamental properties of AlB_2 structured, metastable solid solutions of Si in group IV transition metal diborides, namely TiB_2, ZrB_2, and HfB_2. A particular emphasis was placed on the occupation of different alloying sublattices, influencing the structural integrity of α-type phases in correlation to experimental observations.

2. Methods

2.1. Computational details

3 × 3 × 4 supercells, containing 36 transition metal sites and 72 boron sites, were generated from the primitive AlB_2 prototype (SG 191) TMB_2 unit cell, where TM=Ti, Zr, or Hf. The random alloying of Si was implemented by the Special Quasi-random Structure (SQS) approach [76], making use of the *sqsgenerator* python suit [77]. Si atoms were placed either on the transition metal sublattice or the boron sublattice, respectively. Additionally, mixed sublattice alloying with an equal partitioning of Si on both sublattices was incorporated. Also boron or metal vacancies were introduced into the systems via the SQS technique, by removing boron or transition metal atoms, respectively. For vacancy generation on the alloying sublattice, a removal of pristine and alloying atoms held the silicon content on the regarded sublattice roughly constant.

The calculations in this study are based on DFT, as implemented in the Vienna Ab initio Simulation Package (VASP) [78], which employs the Projector Augmented Wave (PAW) method [79,80]. The PAW potentials were chosen according to their recommended parametrization, as given on the VASP Wiki website [81]. The Generalized Gradient Approximation (GGA) of the electron–electron exchange–correlation potential was utilized, as parameterized in the form suggested by Perdew, Burke, and Enzerhof (PBE) [82]. Following experimental observations, all calculations were run without spin polarization, and Spin-Orbit Coupling (SOC) was not directly taken into account. The Kohn–Sham wavefunctions were expanded via plane waves, while using an energy cutoff of 520 eV. An automatically generated Monkhorst–Pack k-mesh, centered around the Γ-point and utilizing a k-point spacing of 0.1 $Å^{-1}$, was set up for the supercells. A Methfessel-Paxton [83] smearing of 0.2 eV was applied. The structural relaxation was performed by using the *GADGET* python code by Bučko et al. [84], which implements the method of *"lattice internal coordinates"* and allowed for a free movement of all atoms within the supercell. At the same time, the latter was constrained to obey the symmetry of a hexagonal system, namely $a = b$ for the lattice parameters and $\alpha = \beta = 90°$ as well as $\gamma = 120°$ for the corresponding cell angles. The total energy convergence threshold was set to 10^{-5} eV, while the structural relaxation was stopped after reaching a threshold of 10^{-4} eV.

2.2. Experimental

For validation and comparison of the calculated results, experimental data on Ti-Si-$B_{2\pm z}$ and Hf-Si-$B_{2\pm z}$ was taken from a preliminary work by T. Glechner et al. [41]. These single-phased thin films of the latter compounds were deposited by an in-house built PVD system [85]. For further information on the deposition parameters, the determination of sample stoichiometries by Inductively Coupled Plasma Optical Emission Spectroscopy (ICP-OES), and the structural analysis by XRD, we here refer to the original publication [41]. The therein obtained datasets for compositions and diffraction patterns were directly used in this work. Additionally, load–displacement curves, which were obtained through Nanoindentation, were re-evaluated by the method after Oliver and Pharr [86,87], using simulated Poisson ratios to calculate the Young's moduli.

2.3. Evaluation methods

The chemical stability of compounds was evaluated via calculation of their energy of formation, E_f, per atom, defined via:

$$E_f = \frac{E_0\left(\mathrm{TM}_u\mathrm{Si}_v\mathrm{B}_w\right) - uE_0\left(\mathrm{TM}\right) - vE_0\left(\mathrm{Si}\right) - wE_0\left(\mathrm{B}\right)}{u+v+w}, \quad (1)$$

where $E_0\left(\mathrm{TM}_u\mathrm{Si}_v\mathrm{B}_w\right)$ is the total energy of a supercell, with TM=Ti, Zr, Hf and u, v, w are the number of TM, Si and B atoms in this cell, respectively. E_0 (TM), E_0 (Si) and E_0 (B) are the total energies per atom of hcp-Ti, hcp-Zr, and hcp-Hf (all SG 194), diamond-Si (SG 227) and trigonal B (SG 166), respectively.

The structural analysis of the relaxed supercells was carried out through visual inspection, with the help of the program suit VESTA [88], in addition to an analysis of their simulated XRD patterns, also generated with VESTA. Furthermore, Radial Distribution Functions (RDFs) of the supercells and specific elements therein – generated with the help of the python libraries *pymatgen* [89] and *pyscal* [90] – were inspected to obtain structural insights. An analysis of the chemical bonding in the compounds was performed by inspection of the Crystal Orbital Hamilton Population (COHP) of the elements [91,92], calculated with the help of the Local Orbital Basis Suit Towards Electronic Structure Reconstruction (LOBSTER) [93,94]. The latter calculations were based

on the pbeVASPfit2015 basis set, while the COHPs were generated for atoms within a maximum distance of 3.5 Å, which was chosen in order to give a reasonable demand in computational resources, while catching all chemically relevant interactions. An absolute charge spilling below 2% assured a trustworthy projection for all regarded compounds.

The compositional space of defected, silicon alloyed diborides of the type $TM(Si,B)_{2\pm z}$, was examined through the impact of vacancies on the compound's formation energy per atom. Positive z indicates the number of metal vacancies and negative values vacancies on the boron sublattice. An interpolation of the obtained DFT results was carried out, while an inspection of the resulting energies lead to the selection of a third order multivariate polynomial of the form $\sum_{\mu=0}^{3}\sum_{\nu=0}^{3-\mu} a_{\mu\nu} z^{\mu} x_{\mathrm{Si}}^{\nu}$ as fitting function, where x_{Si} is the content of silicon in atomic percent and $a_{\mu\nu}$ are the fitting parameters. Reiterated fitting of the data through an exploration of negligibly small fitting parameters and their dismissal lead to the following final form used as a fitting function for the energy landscape of the composition-vacancy space:

$$\epsilon_f\left(z, x_{\mathrm{Si}}\right) = a\,z^3 + b\,x_{\mathrm{Si}}\,z^2 + c\,z^2 + d\,x_{\mathrm{Si}} + e\,, \tag{2}$$

while in Eq. (2) the variables a, b, c, d and e are fitting parameters. The chemical stability of alloyed compounds could then be analyzed via an interpretation of the function

$$\Delta E_f\left(z, x_{\mathrm{Si}}\right) = \epsilon_f\left(z, x_{\mathrm{Si}}\right) - \epsilon_f\left(0, x_{\mathrm{Si}}\right)\,, \tag{3}$$

which yields negative values of $\Delta E_f\left(z, x_{\mathrm{Si}}\right)$ for a stabilizing, and positive values for a destabilizing nature of vacancies.

Elastic properties were calculated by using a stress–strain method employing the approach proposed by Yu et al. [95]. Therefore, 12 linearly independent strains, which were scaled to possess a maximum component of 2.1% strain, were oppressed on the supercells. Since the elastic matrices C_{ij} obtained lack any symmetry, they were projected onto the closest matrix of a hexagonal symmetry [96], by using an euclidean metric. To estimate the macroscopic elastic properties of a polycrystalline material, the Voigt–Reuss–Hill approximation was used [97, 98]. Directional moduli for systems with hexagonal symmetry were calculated according to the equations given in the Appendix of [99]. The impact of Si alloying on the compound's elastic properties were evaluated with the semiempirical criteria proposed by Pugh [100] and Pettifor [101]. For the G/B values the corresponding Voigt–Reuss–Hill averages were used, and the Cauchy pressure for hexagonal systems was evaluated via the weighted average $\left(2\left(C_{13}-C_{44}\right)+\left(C_{12}-C_{66}\right)\right)/3$, as proposed in [99].

3. Results & discussion

3.1. Energetics and unit cell properties

3.1.1. Energies of formation

Unlike for near-equilibrium bulk solids, synthesizability of compounds by the aid of PVD-based methods usually is characterized by a negative E_f (combined with mechanical and dynamical stability) [102]. While the latter is fulfilled for all metastable states, equilibrium structures have to prove stability against decomposition routes, in the means of endothermic reaction enthalpies. Fig. 1 presents the E_f in relation to the Si content on different sublattices up to a Si content of 66 at. %, representing the disilicide. As can be seen in Fig. 1(a), the compounds feature a different range of soluted silicon that lead to negative E_f, dependent on the sublattice occupied. The boron sublattice, denoted by $TM(Si,B)_2$, is however clearly energetically favored. Even though the compounds appear metastable with respect to unary elements, a decomposition into multi-phase mixtures under thermodynamic equilibrium conditions is expected, according to the convex hull of these ternary systems [103]. Estimated Gibbs free energies of decomposition (see: Fig. S1) turn out negative for both $TM(Si,B)_2$ and $(TM,Si)B_2$, suggested also by annealing experiments of experimental thin films [30,40,42]. Nevertheless, nucleation barrier energies are anticipated to hinder metastable solid-solutions – which can be experimentally acquired through PVD techniques – from decomposition up to critical, but unknown, finite temperatures. Therefore, if drifting far enough from thermodynamic equilibrium conditions, a solubility limit for the metastable state may be explored through a structural destabilization of the AlB_2 type symmetry, which is indicated by crosses in Fig. 1. The aforementioned structural destabilization will be object of in-depth investigations later on in this study.

Focussing now on the priorly defined metastable solubility limit, from Fig. 1(a) an immediate destruction of the AlB_2-type, for combined Si occupation on both sublattices, is observable. In contrast, a low amount of Si is soluble in the α-type structure, when placed on the transition metal sublattice, see Fig. 1(b). Nevertheless, silicon occupation on the boron sublattice clearly combines an energetical preference, in the means of lowest E_f, with a long-lasting structural integrity of an AlB_2 type phase. This leads to estimated metastable solubility limits of 24 at. %, 27 at. %, and 25 at. % Si in $Ti(Si,B)_2$, $Zr(Si,B)_2$, and $Hf(Si,B)_2$, respectively. In contrast to that, only contents of 8 at. %, 5 at. %, and 2 at. % Si are soluble on the metal sublattice of $(Ti,Si)B_2$, $(Zr,Si)B_2$, and $(Hf,Si)B_2$, obtaining a metastable α-type structure in the relaxed state.

3.1.2. Lattice parameters

In Fig. 2 the evolution of the a and c lattice parameters of the different hexagonal cells is depicted. Since mixed sublattice alloying lead to an immediate loss of the α-type symmetry, these data points are excluded from the following discussion. For both sublattice alloying on the metal (half-filled hexagons) and boron sites (open hexagons), the change of the c lattice parameter is comparably low (in the range of 0.1 Å) in the stable region, obtaining an AlB_2 structure, see Fig. 2(a). Nevertheless, the expansion in the c direction is more pronounced for compounds of the type $(TM,Si)B_2$ than for the energetically preferred $TM(Si,B)_2$ comparing the same amount Si. The a lattice parameters, shown in Fig. 2(b), undergo a distinct expansion when Si is placed on the B sublattice, (about 0.2 Å), for all alloyed diborides, respectively. In case of the energetically unpreferred metal sublattice occupation, even a contraction of a is observed for $(Zr,Si)B_2$ and $(Hf,Si)B_2$, whereas it remains fairly constant for $(Ti,Si)B_2$. The cell volumes therefore show a continuous increase for Si alloying on the boron sublattice, while little to no changes are predicted for the case of soluting silicon on the transition metal sublattice.

Above findings may be verified via employing an easy model based on atomic radii, r, of the chemical elements, by assuming $r(\mathrm{B}) < r(\mathrm{Si}) \ll r(\mathrm{TM})$, respectively. Since the a lattice parameter spans the B-B and TM-TM sheets via the 100- and 010-directions, an introduction of smaller Si atoms into metal planes presumably leads to a contraction. However, in the boron planes it may lead to an adaption to higher bond distances due to the incorporation of bigger Si atoms within B sheets.

Combining E_f and structural stabilities of α-type compounds in Fig. 1, a random alloying of Si – similar to PVD growth processes – can be expected to prefer the boron sublattice. While finite temperature corrections to the Gibbs free energies will barely impact our regards on metastability, vacancies are anticipated to do so. Therefore, the following chapters will at first investigate ideal and later on defected compounds of the type $TM(Si,B)_{2\pm z}$.

3.2. AlB_2 -type phase destabilization

During the constrained relaxation of the hexagonal supercells, movements of the atom positions within the cell were allowed freely. A visual inspection of the cells led to the insight that for each distinct alloying sublattice, a substantial loss in symmetry was apparent when a certain content of Si was exceeded. Even though a driving force for decomposition was a priori expected from equilibrium phase diagrams,

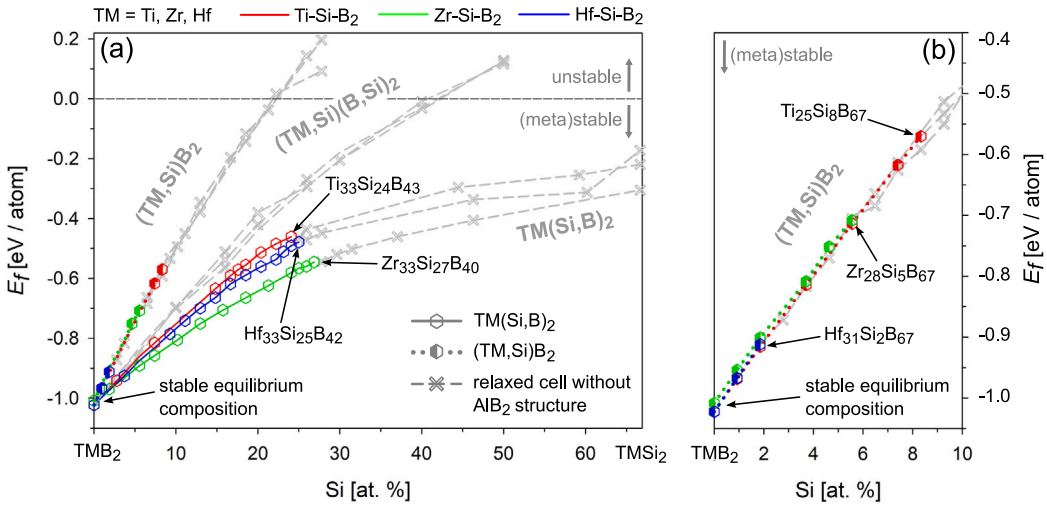

Fig. 1. Calculated E_f per atom, plotted over the Si content in at. % on different sublattices. Ti-Si-B_2, Zr-Si-B_2, and Hf-Si-B_2-based compounds are indicated in red, green, and blue respectively. Hexagons indicate data points, that possessed a cell with AlB_2 symmetry, while crosses did not. For better readability, not all data points that construct the underlying linear interpolation are shown. Alloying on the metal, boron or both sublattices is indicated by the notations (TM,Si)B_2 (half-filled hexagons), TM(Si,B)$_2$ (open hexagons), and (TM,Si) (B,Si)$_2$ respectively. (a) Overview of the E_f for different sublattice alloying of Si. (b) Zoom-in of cells where Si was only placed on the transition metal sublattice. In both (a) and (b), arrows indicate thermodynamically stable equilibrium compositions, and those possessing the highest silicon content that could be sustained in a metastable structure of AlB_2 type. For interpretation of the color references in this figure legend, please refer to the web version of this article.

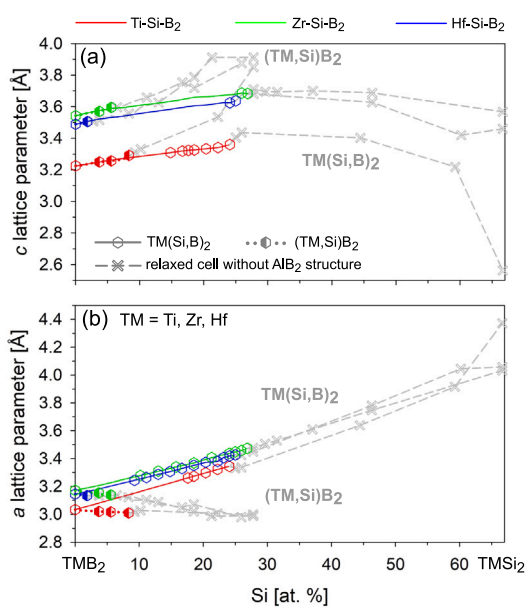

Fig. 2. Evolution of the (a) c lattice parameter and (b) a lattice parameter over the silicon content, for alloying on different sublattices of the regarded transition metal diborides. The symbols and color-code used are identical to Fig. 1. Not all datapoints that construct the underlying linear interpolation are shown.

the explored breakpoint for massive structural distortion seemed non-trivial. At alloy contents around this border a massive clustering of Si atoms, in combination with strong out of plane movement of transition metal atoms and in-plane displacements of B atoms occurred. A schematic visualization of this finding, compromised by a Hf(Si,B)$_2$ compound with 17 at. % Si, sustaining the α-type, and one with 31 at. % Si, which was highly distorted, is shown in Fig. 3(a). With the help of statistical methods, which will be the point of the following discussion, investigations of this cell distortion allowed to extract metastable solubility limits of Si in AlB_2 structured transition metal diborides.

3.2.1. Statistics of the SQS cell distortion

In order to extract solubility limits in the metastable state by statistical methods, sets of 5 different SQS supercells, with the same number of silicon atoms, were generated and relaxed in a DFT calculation for a broad range of Si contents around the expected range of observed clustering initiation. Fig. 3(b) depicts the ratio of relaxed cells sustaining the α-type, in relation to their Si content, for the case of Hf(Si,B)$_2$ and (Hf,Si)B_2. For Si occupation on the metal sublattice, a change of not even 1 at. % Si lead to a massive drop in structural stability of α-structured cells after alloying beyond 2 at. %. Therefore, a very rigid metastable solubility limit for AlB_2-type compounds could be defined. For the (Ti,Si)B_2 and (Zr,Si)B_2 system in Fig. S2(a) and Fig. S3(a), analogous drops in relaxed α-type cell ratios are apparent, just that the latter are encountered beyond 8 at. % Si and 5 at. % Si, respectively. For the case of boron substitution, which has already been spotted as the physically more relevant case, a rather smooth but steep transition from 100 to 0 percent of relaxed SQS cells, sustaining the α structure, could be detected. This transition is taking place in a narrow range around 25 at. % Si. Therefore, a definition of the metastable solubility limit via a threshold, where 50% of all regarded SQS cells were of AlB_2 type, should lead to rather solid values for all investigated TM(Si,B)$_2$ systems, with a deviation of 1–3 at. % Si.

In Fig. 3(c), the scattering of formation energies, with respect to their arithmetic mean values, and their respective standard deviations, are depicted for several sets of SQS cells with different Si content in (Hf,Si)B_2. The datapoints also contain information on their relaxed cell geometries, and it is straightforward to conclude that just from an energetic standpoint no clear indication for high or low distortion of specific SQS instances is visible. It can however be concluded, that with decreasing ratio of relaxed cells of α-type, the E_f show a higher scatter, which may be directly related to the observed clustering behavior. The latter manifests itself in an increasing extent of the error bars of roughly 3 meV/atom to 15 meV/atom within a change of ≈ 5 at. % Si. Similar trends are observable in the case of (Ti,Si)B_2 and (Zr,Si)B_2, in Fig. S2(b) and Fig. S3(b), respectively. In Fig. 3(d) a similar plot is shown for the case of boron sublattice alloying, and also here no clear trend – regarding a coupling of E_f to cell distortion – is apparent. For alloy contents around the proposed AlB_2 structure destabilization limit, the error bars of the data points stay in a rather high, but stable range of around 5–18 meV/atom. Again, similar behavior is encountered for Ti(Si,B)$_2$ in Fig. S2(c) and Zr(Si,B)$_2$ in Fig. S3(c). Even

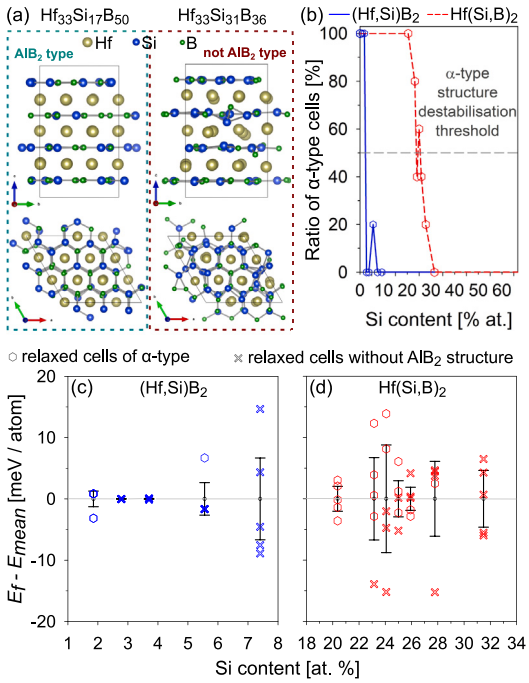

Fig. 3. (a) Relaxed geometries of $Hf(Si,B)_2$-based compounds, with silicon contents of 17 at. % and 31 at. %, which were below and above the proposed AlB_2 structure destabilization limit, respectively. (b) Ratio of relaxed supercells with AlB_2 type structure, for sets of 5 different, Hf-Si-B_2-based, SQS generated initial structures with the same content of Si. (c) Deviation of the cell formation energies with different Si content in $(Hf,Si)B_2$, to their arithmetic mean values $E_f - E_{mean}$, with respective standard deviations. Data points with a relaxed cell of AlB_2 type are shown as hexagons, while others are depicted as crosses. (d) Statistical data for the case of $Hf(Si,B)_2$, based on 5 different cells per fixed silicon content, illustrated in the same way as in Fig. 3(c).

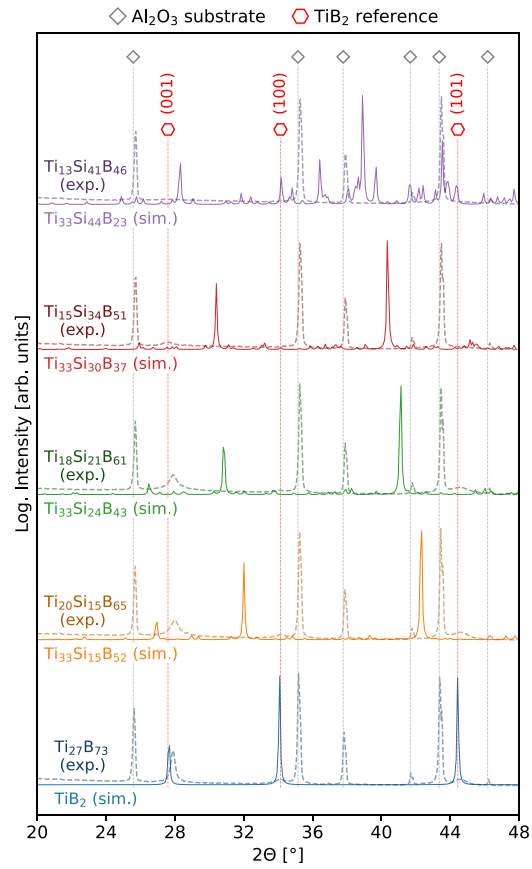

Fig. 4. Simulated XRD patterns of $Ti(Si,B)_2$-based compounds, as well as experimental diffractograms of highly 001-oriented, DCMS deposited Ti-Si-$B_{2\pm z}$ thin films on saphire (Al_2O_3) substrate, taken from [13]. Their compositions are indicated on the left-hand side below or above the corresponding simulated (sim.) or experimental (exp.) XRD pattern, respectively. Experimental reference reflections of Al_2O_3, as well as of TiB_2, are accentuated through dotted lines and indexed for the binary diboride. To increase the readability, simulated diffractograms are depicted as Lorentz-functions with a Half-Width at Half-Maximum (HWHM) of 0.1 and their relative intensities were cut off at a maximum value of 40 percent.

though the observed scatter in E_f is fairly low when compared to thermal energies, a limited rigidity of formation energies, obtained from distorted SQS-cells, should be taken into account, if chemical stabilities are considered.

The statistical approach described above allows to fixate a solubility limit in the metastable state, just by means of the structural distortion of relaxed supercells. Therefore, in the following the structural chemistry of Si in group IV transition metal diborides will be investigated, and methods to categorize a cell as α-type or otherwise will be elaborated on.

3.2.2. Comparison of experimental and simulated XRD patterns

A comparison of simulated and experimentally obtained XRD patterns for theoretically described $Ti(Si,B)_2$-based compounds and deposited Ti-Si-$B_{2\pm z}$ thin films, is depicted in Fig. 4. For the binary diboride, the 2Θ positions of the reference reflections match very well with both the simulated and experimental patterns. In the latter case, the presence of residual (compressive) stresses, due to the deposition process, may lead to the observed shift of the 001-peak to higher 2Θ angles. Since the scaled intensities of the simulated compounds were cut off above 40 % for better readability, only the height of 001-peaks will be discussed in the following. It is worth to note, that simulated patterns do only persist a finite width due to their illustration through Lorentz-functions, and therefore no comparison with experimental results, as for example the Full Width at Half Maximum (FWHM) of the peaks, can be made.

From the simulated XRD patterns of $Ti(Si,B)_2$ in Fig. 4, a continuous, pronounced shift of the 100- and 101-peak towards lower 2Θ angles with increasing Si content is apparent. This is in line with the strong increase of the a lattice parameters, as discussed in Fig. 2. The 001-reflections show substantially smaller peak shifts, combined with decreasing intensities when exceeding the proposed AlB_2 structure destabilization limit of 24 at. % Si in $Ti(Si,B)_2$, underlining prior insights on the evolution of the c lattice parameters. The structural destabilization of a metastable, random alloy phase of the hexagonal diboride with silicon contents above 24 at. % is also apparent from multiple emerging small peaks that may not be related to the TiB_2 reference in any way. This effect is already visible at 24 at. % of Si and becoming even more pronounced at higher contents, see the top most pattern. Even though the decrease in intensity of the 001-reflection, with respect to increasing alloying content, does fit the experimental results, the observed peak shifts fail to do so. The observation that experimental diffractograms exhibit minimal variation in 2Θ angles across an alloy content range of approximately 40 at. % Si, reinforces criticism towards commonly published average film compositions, consolidating the need for high-resolution 3D chemically resolved analysis techniques.

From just comparing experimental and simulated XRD-patterns, and under the assumption that indeed metastable solid solutions were experimentally achieved, one has to conclude that less than 15 at. % Si are persistent in the crystalline phase of the thin films under investigation. The residual silicon, accounting for the measured total film composition, then has to be segregated in additional amorphous phases or the grain boundary interior, leading to an inhomogeneous over all distribution of Si.

Nevertheless, the discrepancies between simulated and experimental XRD patterns may partially be ascribed to high defect concentrations, such as of vacancies and dislocations, which are expected to be present in PVD thin films, but were not incorporated in the simulations.

Since above observations on the peak shifts, coupled to the evolution of lattice parameters, as well as on the decreasing intensities of the 001-peak, also apply for $Zr(Si,B)_2$ and $Hf(Si,B)_2$, they are not further discussed in this work.

3.2.3. Analysis of the radial distribution functions

In order to obtain even further insights into the clustering behavior of the different chemical species in the Si alloyed $TM(Si,B)_2$, the total Radial Distribution Functions, as well as the partial RDFs of Si, B, and the transition metal, of unrelaxed and relaxed SQS cell geometries were compared in Fig. 5. From the total RDFs of $TM(Si,B)_2$ compounds in Fig. 5(a), (b), and (c) it is clearly visible that, upon structural relaxation, the unrelaxed histogram pattern is undergoing a substantial dispersion of the initial B-B next neighbor (NN) peak at ≈ 1.8 Å and the B-TM NN-peak at ≈ 2.4 Å (TM=Ti) or ≈ 2.5 Å (TM=Zr, Hf), respectively. In addition to that, beyond the TM-TM NN peak at ≈ 3 Å (TM=Ti) or ≈ 3.2 Å (TM=Zr, Hf), intense broadening of the RDFs is visible, leading to a loss of long range order at Si contents above 15 at. %. From their respective partial RDFs it is observable that transition metal atoms undergo excessive orderless displacement from their initial position, accompanied by a collective drift apart from each other. This effect leads to an increased mean bond distance of the metal species. Both observations are more pronounced for high Si amounts. By analyzing the partial RDFs of boron atoms for all compounds, an undirected displacement of the B atoms from their initial position is evident. This feature is more pronounced for higher contents of Si, while their mean B-B next neighbor distance stays almost the same, at least until a destabilization of the AlB_2 type structure takes place around ≈ 30 at. % Si. Furthermore, the Si atoms undergo an initial adaptation to a bond distance of ≈ 2.1 Å even at low alloying contents of 7 at. %, which is evident from the partial RDFs of these species. However, further deviations from this bond distance stay low until the α-type structure is destabilized. If the metastable solubility limit is surpassed, for all compounds a further shift of the mean Si-Si bond distance to roughly 2.4 Å is apparent, accompanied by a broadening of the respective silicon RDFs. Since the NN distance in diamond structure Si is also ≈ 2.4 Å [104], and (due to technical reasons) the equilibrium decomposition products suggested in Fig. S1 are unlikely to arise in a relaxation of the employed unit cells, the shift indicates a structural destabilization due to Si clustering. The latter was also evident in Fig. 4 from arising non-indexable peaks in the simulated XRDs, which were not observed in metastable $TM(Si,B)_2$ compounds below the solubility limit, possessing a Si-Si bond distance of ≈ 2.1 Å.

3.2.4. Chemical bonding analysis through COHP

In Fig. 6 the COHP, as well as the partial Crystal Orbital Hamilton Populations, denoted as pCOHP(A-B), where A and B are the respective chemical elements of the specific interaction, are shown for compounds of the type $Hf(Si,B)_2$. By examining a compound with a low alloy content of 4 at. % Si in Fig. 6(a), we observe a fully positive pCOHP(Hf-Si) up to 2 eV above E_F, indicating a thoroughly bonding nature of the transition metal interaction with silicon, even at finite temperatures. Pronounced bonding states may also be observed in pCOHP(Si-B). However, around ≈ 3 eV below the Fermi energy, anti-bonding states of low intensity are apparent. The latter start to get more distinct at E_F, indicating an expected destabilization followed by decomposition at sufficient temperatures. Similar observations can be made for the case of $Ti(Si,B)_2$ with 3 at. % Si and $Zr(Si,B)_2$ with 4 at. % Si, in Fig. S4(a) and Fig. S5(a), respectively. Due to the low alloy content, the contribution of pCOHP(Si-Si) to the total COHP is negligibly small for all three systems, and no comparison to diamond-Si is possible.

If the content of soluted Si in $Hf(Si,B)_2$ is increased to values of 15 at. %, it is effect on the chemical bonding is clearly visible, see Fig. 6(b). The bonding nature of pCOHP(Hf-Si) increases in intensity, especially for energies around E_F, while the overall maximum lies at roughly −4 eV. For Ti-Si-B_2 and Zr-Si-B_2 based systems in Fig. S4(b) and Fig. S5(b), interactions of the transition metals with silicon show likewise behavior. The cohesive interaction of Si with B, up to ≈ 3 eV below the Fermi energy, gains intensity for all three compounds, while its anti-bonding part is especially pronounced around E_F and at energies beyond. For the less intensive Si-Si interaction, similar bonding natures are apparent in those intervals, but no similarity to the COHP of diamond-Si may be found.

Regarding quantum chemistry, changes in stability of α-type solid solutions depend on the alloy content, which governs the balance of bonding pCOHP(TM-Si) and anti-bonding pCOHP(Si-B) and pCOHP(Si-Si) interactions, respectively. For example, weakened bond strength within the hexagonal sheets, compromised of Si and B atoms, accompanied by an elongation of bond distances, were already expected from the increase in a lattice parameters in Fig. 2. The RDFs of Si and B atoms in Fig. 5 also lead to the insight, that Si adapts to higher bond distances, and its incorporation expands the basal plane. Both this observations are explained through the arisal of anti-bonding pCOHP(Si-B) and pCOHP(Si-Si) states at E_F and above, that would be occupied at smaller unit cell volumes i.e. higher orbital overlap. Most likely an incompatibility of sp^3-hybridized silicon with the mixed sp^2-sp^3 boron layers gives rise to the anti-bonding character of this interaction. Nevertheless, already from low variations in c lattice parameters and extensive movements of metallic species, visible from their RDFs, a stabilizing factor was expected from the Si-TM interactions. High intensity peaks of pCOHP(TM-Si) below E_F, stemming from bonding interactions of d-metal orbitals with those of sp^3-hybridized silicon, very prominently acknowledges this prior assumption. Therefore, the overall cohesive energy may decrease due to alloying with silicon, which is known from the behavior of E_f in Fig. 1, but the intense bonding nature of states way below E_F still prevent a structural destabilization of the α-type, which was the guiding phenomenon for proposed metastable solubility limits.

In Fig. 6(c) the COHP curves for a $Hf(Si,B)_2$-based compound with a silicon content of 25 at. % are depicted, which represents the AlB_2 structure type destabilization limit. A further intensification of anti-bonding Si-B states around E_F is apparent, which become even more pronounced above the Fermi energy. From the pCOHP(Si-Si) curve both a gain in bonding states at energies below ≈ −3 eV, with respect to the Fermi energy, and of anti-bonding states above this energy, are evident. Even though a high similarity of pCOHP(Si-Si) and pCOHP(Si-B) is apparent, in analogy to diamond-Si, the lowest energy states, as well as states around E_F, show suppressed intensity for pCOHP(Si-Si). The pCOHP of transition metal atoms with silicon shows a further enhanced intensity, while its maximum is shifted to energies above −4 eV, compared to 16 at. % Si. Furthermore, the bonding states around E_F undergo a steep transition to anti-bonding nature around 1 eV above the Fermi energy. Since strong similarities are again observed for the case of Ti-Si-B_2 and Zr-Si-B_2 based systems in Fig. S4(c) and Fig. S5(c), no additional insights can be found for those. However, for $Hf(Si,B)_2$ and $Zr(Si,B)_2$ the total COHP already shows a drastic change from bonding to anti-bonding nature right below the Fermi energy, at this content of silicon, which is only encountered at E_F for $Ti(Si,B)_2$. Even though this observation already hints towards an emerging loss in chemical stability, structural concerns support high Si contents around 25 at. % to be soluble in metastable α-type compounds. Furthermore, bonding TM-Si states are very pronounced around the Fermi energy, whereas unoccupied anti-bonding Si-B states lie above E_F, which is in line with an expected decomposition at finite temperatures. Also, the anti-bonding pCOHP(Si-Si) are of low intensity, therefore an intermediate Si-Si bond distance of ≈ 2.1 Å in the α-type was discovered in Fig. 5.

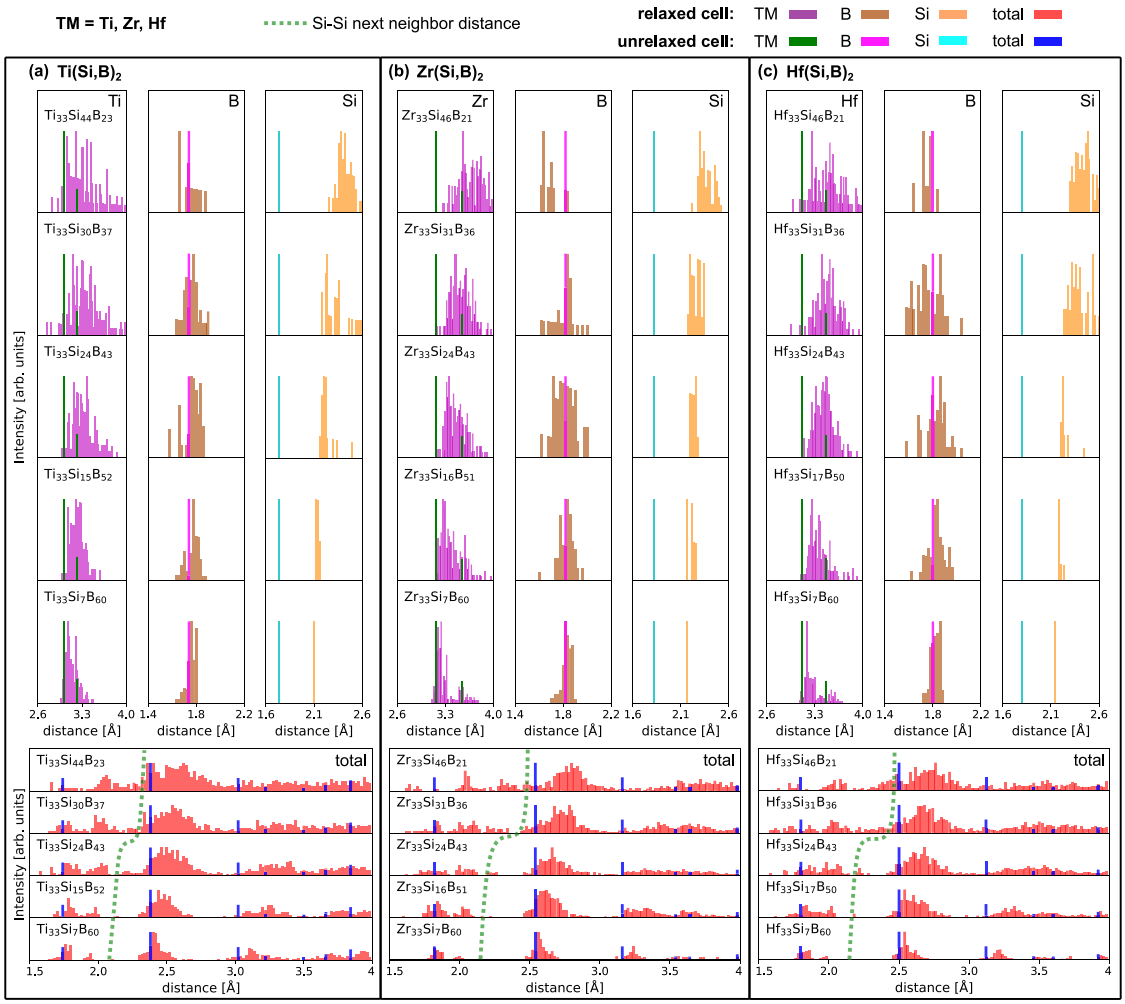

Fig. 5. Simulated Radial Distribution Functions of unrelaxed and relaxed cells of (a) $Ti(Si,B)_2$, (b) $Zr(Si,B)_2$, and (c) $Hf(Si,B)_2$, with varying Si contents. The top of each subfigure shows the partial RDFs of the corresponding transition metal, boron, and silicon atoms, respectively. On the bottom of each subfigure the total RDFs are shown. For each plot, a number of 150 bins were used to construct the histogram bars in the region between 1 Å and 4 Å. For the total RDFs, the dotted green line, constructed through the peak of the partial Si RDFs, acts as a guide for the eye, indicating the evolution of the observed mean Si-Si next neighbor distance. The color-code for the histograms of relaxed and unrelaxed cells is the same for the RDFs of transition metal, boron and silicon atoms as well as for the total RDFs, in all subfigures.

When inspecting the COHP curves of non α-type $Hf(Si,B)_2$ with 46 at. % Si depicted in Fig. 6(d), or $Ti(Si,B)_2$ with 44 at. % Si and $Zr(Si,B)_2$ with 47 at. % Si, in Fig. S4(d) and Fig. S5(d), respectively, a strong similarity of pCOHP(Si-B) and pCOHP(Si-Si) is apparent. For them, anti-bonding states of high intensity persist above −3 eV, while only the low energy bonding states of Si-Si show increased intensity, compared to compounds with lower amounts of silicon. However, the low energy bonding states of Si-B show little to no change. The observed clustering of Si atoms fits in this picture, as their pCOHP indicates a strong cohesive interaction. Nevertheless, even at this high content of Si, no clear similarity of pCOHP(Si-Si) with the COHP in diamond-Si is evident, emphasizing the discrepancy in chemical bonding. From pCOHP(Hf-Si) and pCOHP(Zr-Si), a shift of bonding states located around E_F towards the intense maximum around −3 eV is evident, while states above the Fermi energy show a steep transition towards anti-bonding nature. For pCOHP(Ti-Si) the overall trend is the same, just that the maximum is of less intensity, but in return broader. For all three systems, low energy bonding states experience a further increase in intensity when compared to Si contents around 25 at. %, however less pronounced than for the case of pCOHP(Si-Si). For $Zr(Si,B)_2$, occupied anti-bonding states of the total COHP at −1 eV are encountered, which is not the case for $Hf(Si,B)_2$ and $Ti(Si,B)_2$. Nevertheless, high intensity anti-bonding states far below E_F are apparent for all three systems, indicating a destabilization of AlB_2 structured compounds.

3.3. Mechanical properties

In the following section, the mechanical properties, calculated from a stress–strain method by relaxing SQS supercells in VASP, will be discussed. All investigated compounds were mechanically stable.

3.3.1. Elastic moduli of alloyed compounds

The directional Young's moduli, within the 001-plane (E_{010}) and in the 001-direction (E_{001}), of $Ti(Si,B)_2$, $Zr(Si,B)_2$ and $Hf(Si,B)_2$ of various Si contents are depicted in Fig. 7(a). A continuous decrease of both E_{001} and E_{010} is apparent, while the stiffer 010-direction shows a steeper drop of its elastic modulus. Both directional moduli share the same rate of reduction for all regarded transition metals. While E_{010} takes values of 520–620 GPa for the binary diborides, at 25 at. % of Si only roughly 180-210 GPa are reached. The lower values for E_{001} of around 390–420 GPa for binaries undergo a less pronounced drop to values in the range of 150–190 GPa. This is in line with the observed decrease in bond strengths within the basal plane, compromised of Si and B atoms, while the TM-Si interaction was mainly of bonding type. Thus, at high silicon contents of 25 at. % both the in-plane and out of plane modulus are of roughly the same magnitude. These

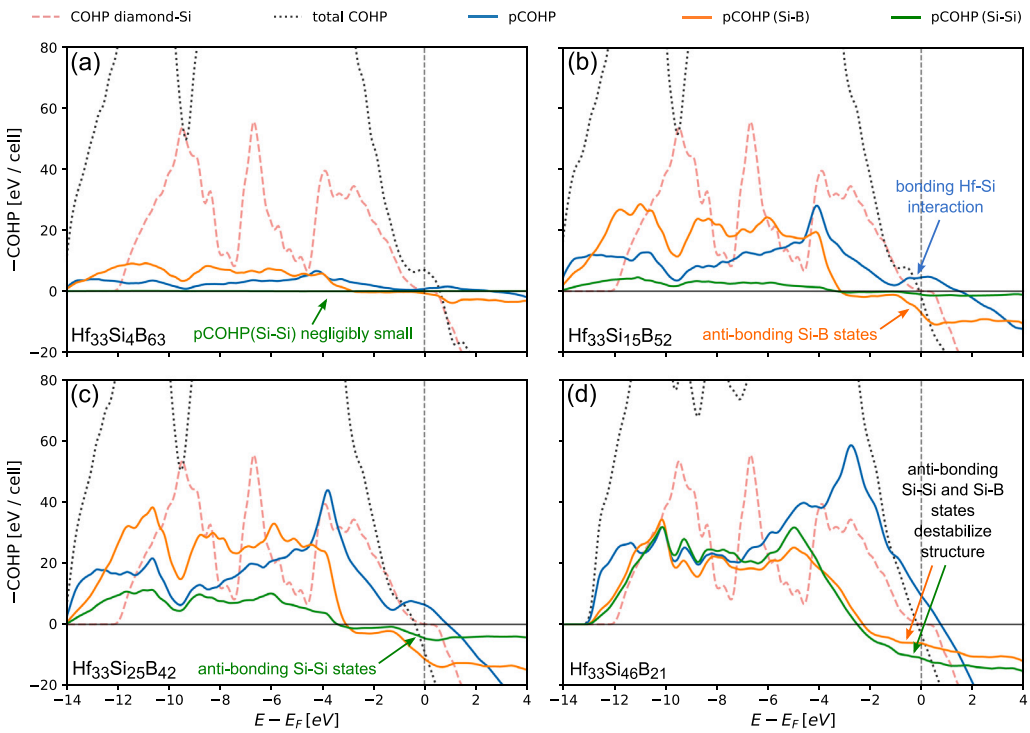

Fig. 6. Crystal Orbital Hamilton Populations of $Hf(Si,B)_2$-based compounds with (a) 4 at. %, (b) 15 at. %, (c) 25 at. %, and (d) 46 at. % Si. For comparison, the total COHP in diamond-Si is depicted in all subfigures. The energy difference $E - E_F$ of the corresponding states, with respect to the Fermi energy E_F, is given on the horizontal axis. The inverted COHP is given on the vertical axis, in order to assign bonding states positive, and anti-bonding states negative −COHP values. Due to their high relevance for this study, only the interactions of Hf with Si, pCOHP(Hf-Si), of Si with B, pCOHP(Si-B), and of Si with Si, pCOHP(Si-Si) are depicted for the case of $Hf(Si,B)_2$. Additionally, the total COHP of the latter compounds is also shown. Especially relevant parts of the COHP curves are indicated by arrows, in combination with short descriptive comments.

observations presumably indicate a transition from hexagonal to more isotropic material behavior, stemming from the hybridization of Si-sp^3 with TM-*d* orbitals, which leads to an increased metallic character of the chemical bonds.

In Fig. 7(b) the Voigt–Reuss–Hill average of the Young's moduli E_{VRH} are compared to the experimental indentation moduli of Ti-Si-$B_{2\pm z}$ and Hf-Si-$B_{2\pm z}$ thin films. Even though often viable comparisons of E_{VRH} with the measured nanoindentation moduli of thin films are reported in literature [105–107], here some discrepancies are observable. In the binary case, the experimental data of $HfB_{2.36}$ compares well with the corresponding E_{VRH}, whereas for $TiB_{2.72}$ a difference of about 120 GPa is apparent. However, this discrepancy may be explained by the high off-stoichiometry of this thin film, supposably stemming from high volume contents of the tissue phase and defects, leading to a deficiency in metal atoms. Around 15 at. % Si a good match of E_{VRH}, with respect to the experimental data, is observable. Therefore, taking the incomparability of the binary $TiB_{2.72}$ into account, a good match of DFT results with experimental data can be expected at low alloy contents, also for $Zr(Si,B)_2$. From the insert a steady increase of ν_{VRH}, with respect to increasing alloy content, is observable, reducing evaluated indentation moduli at high Si alloying. Nevertheless, when comparing simulation data of $TM(Si,B)_2$ compounds of high Si contents above 15 at. % with the experimental films, increasing deviations are apparent. This may not only be explained by the decreased crystallinity of these samples, which was observable in their XRD patterns, but also their high B/TM ratios, indicating high off-stoichiometries [41].

The Voigt–Reuss–Hill average of the bulk modulus B_{VRH} and of the shear modulus G_{VRH} of the same compounds are shown in Fig. 7(c). A steep decrease of G_{VRH}, from 230–260 GPa to 50–80 GPa is apparent, while the shear modulus may directly be related to the hardness [108]. This is in line with the observed, distinct drop in hardness of Si alloyed diboride thin films with increasing silicon contents, as seen in [37,41,109]. The reduction of B_{VRH} is less pronounced, while values of 240–250 GPa for the binary compounds decreases to 170 GPa for alloying contents of 25 at. % Si.

3.3.2. Influence of Si alloying on the brittleness

In Fig. 8 the G/B ratio versus the Cauchy pressure of $Ti(Si,B)_2$, $Zr(Si,B)_2$, and $Hf(Si,B)_2$-based compounds of various Si contents are depicted. The suggested transition from ductile to brittle behavior, proposed by Pugh and Pettifor, are indicated. Here, the authors want to emphasize, that these criteria were developed for bulk metals, and therefore an application to ceramic materials may be inappropriate [110]. Nevertheless, their appliance for ceramic-based thin films has resulted in fair predictions of the expected impact on ductility of metastable alloy phases [111,112]. According to the underlying indicators, a clear transformation towards ductile behavior can be expected with increasing Si contents. The latter may again be explained through the observed increase in metallic character of bonds between metal and non-metal species. While the binary group IV transition metal diborides are located in a region of predicted strong brittle behavior, according to both the criteria by Pugh and Pettifor, a Si content of 20 at. % already should yield ductile behavior for $Ti(Si,B)_2$ and $Hf(Si,B)_2$. For $Zr(Si,B)_2$ however, an amount of 21 at. % Si still leads to a data point, located in a brittle region. At even higher silicon contents, near the proposed AlB_2 type structure destabilization limit, a clear increase in ductile behavior may be expected, especially when compared to the binary diborides.

Diboride-based thin films synthesized via PVD typically obtain a characteristic columnar microstructure containing an amorphous tissue phase. This tissue phase is the main morphological object where crack propagation and fracture are observed [11,113]. Therefore an increase in ductility of the 001-oriented, crystalline diboride phase, due to the metastable incorporation of Si, might have a negligible impact on the experimentally determined K_{Ic} values. However, an enrichment in silicon is suggested to obtain an impact on the fracture properties of the tissue phase if present, and hence in combination to that of the total thin film.

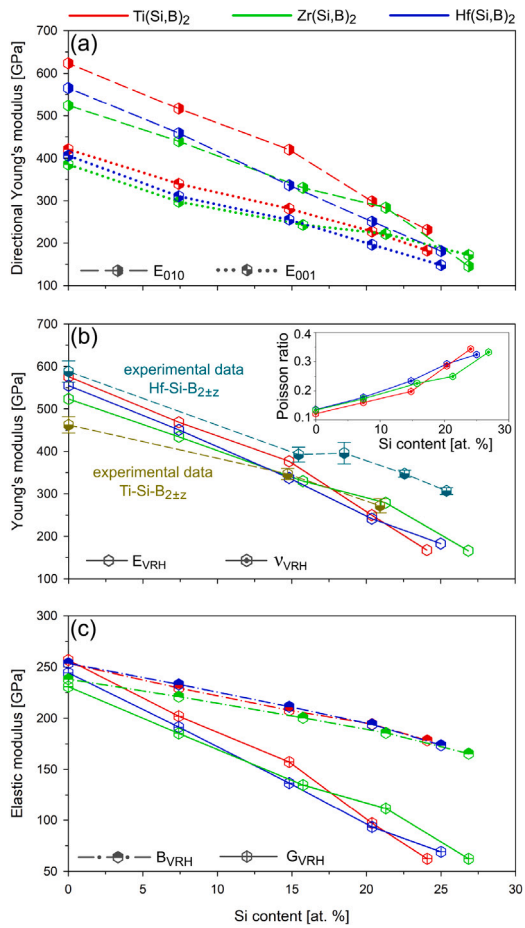

Fig. 7. Elastic moduli of $Ti(Si,B)_2$, $Zr(Si,B)_2$, and $Hf(Si,B)_2$, respectively. (a) Directional Young's modulus within the 001-plane, E_{010}, and in the 001-direction, E_{001}. (b) Voigt–Reuss–Hill average of the Young's modulus E_{VRH} and experimentally determined indentation moduli of Ti-Si-$B_{2\pm z}$ and Hf-Si-$B_{2\pm z}$ thin films, re-evaluated from [41], by using the Voigt–Reuss–Hill averaged Poisson ratios ν_{VRH}, which are shown in the insert. (c) Voigt–Reuss–Hill averages of the bulk modulus B_{VRH} and of the shear modulus G_{VRH}, respectively.

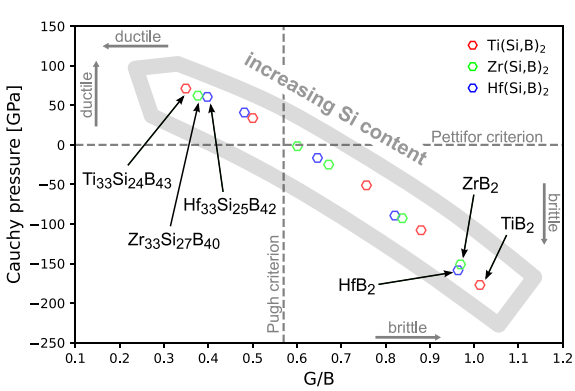

Fig. 8. Cauchy pressure versus G/B ratio of $Ti(Si,B)_2$, $Zr(Si,B)_2$, and $Hf(Si,B)_2$ compounds for various contents of Si. The brittleness criteria by Pugh, predicting a transition from ductile to brittle behavior above G/B ratios of 0.571, and Pettifor, which correlates negative Cauchy pressures to brittle material behavior, are indicated via dashed lines. Arrows mark diborides at equilibrium composition and those with the highest Si content soluble in metastable α-type compounds.

3.4. Phase maps of defected compounds

Since sputter deposited thin films not only are able to persist as metastable solid solutions, but also exhibit extreme defect densities, two-dimensional vacancy phase maps of silicon alloyed diborides are presented in the following.

In Fig. 9(a), (b) and (c) the impact of vacancies on the E_f of $Ti(Si,B)_{2\pm z}$, $Zr(Si,B)_{2\pm z}$, and $Hf(Si,B)_{2\pm z}$-based compounds are depicted, while z describes the number of vacancies on the metal or boron sublattice, respectively. By examining the vacancy-energetics of $Ti(Si,B)_{2\pm z}$ in Fig. 9(a), a steep increase of E_f through an elevating introduction of boron and metal vacancies is visible for the binary diboride. A similar trend was also reported in other publications [47,73], for $TiB_{2\pm z}$, $ZrB_{2\pm z}$, and $HfB_{2\pm z}$, respectively. While the same trend for a reduction in chemical stability is persistent, if the amount of Si in the compound is increased, the energetic influence of vacancies on the boron or metal sublattice is diminishing. This effect may be recognized from the reduced density in contour lines, if two horizontal profiles of a constant Si content are compared. Beyond 5 at. % of Si, the introduction of Ti vacancies is accompanied by a loss of the α-type structure, whereas for 25 at. % Si a metastable $Ti(Si,B)_{2\pm z}$ compound of AlB_2-type may be sustained up to 0.1 vacancies per formula unit on the boron sublattice. When moving away from the equilibrium binary composition, in metastable alloy phases the lowest E_f values are encountered for undefected $Ti(Si,B)_2$ up to 20 at. % of silicon. For higher alloyed compounds in the α-type stable region, vacancies on the boron sublattice become more favorable (stabilizing effect of 10 meV/at. for $z = -0.1$), visualized through the line of *preferred metastable composition* in Fig. 9. However, this impact on the formation energy is relatively insignificant if compared to the observed scatter in E_f induced by the SQS approach, discussed in Section 3.2.1. Furthermore, a finite probability for finding a non-AlB_2 cell in the structurally stable region, for example in $Ti(Si,B)_{2\pm z}$ or $Hf(Si,B)_{2\pm z}$ with 20 at. % Si and $z = -0.1$ or respectively $z = -0.2$, is observable. This is accounted for by the statistical manner of $TM(Si,B)_2$ compound destabilization, initiated through silicon clustering, discussed in Section 3.2.1 and applicable also to defected compounds.

The vacancy-energetics of $Zr(Si,B)_{2\pm z}$-based compounds in Fig. 9(b), similarly to $Ti(Si,B)_{2\pm z}$, show a diminishing impact of vacancies on E_f, with increasing silicon content. However, the impact of Zr vacancies on the chemical stability is more severe than for those of the boron type, which is recognizable from the asymmetric shape of the contour plot. An introduction of vacancies on the Zr sublattice leads to a destabilization of α-type compounds, beyond Si contents of 10 at. %, whereas vacancies on the boron sublattice lead to no structural destabilization. At high alloy contents of 26 at. % Si, the introduction of 0.3 vacancies per formula unit on the boron sublattice even make a small reduction of E_f by 10 meV/at. observable. The latter is however again overshadowed by the error bars encountered in the SQS approach.

Similar observations are apparent for the vacancy-energetics of $Hf(Si,B)_{2\pm z}$ based compounds, as depicted in Fig. 9(c). A less pronounced impact of vacancies on E_f at high alloy contents, accompanied by a minimal energetic stabilization at $z = -0.3$ and 25 at. % Si, are evident. Furthermore, α-type $Hf(Si,B)_{2\pm z}$ shows no destabilization with respect to vacancies on the boron sublattice, whereas Hf vacancies lead to an instability of AlB_2-type structured compounds beyond 10 at. % Si. Highly Hf-deficient structures of 0.3 metal vacancies may not persist in the α-type, even at low silicon contents below 5 at. %.

From above discussion, a descending energetical impact of vacancies on the E_f of metastable TM-Si-$B_{2\pm z}$, with respect to increasing Si contents, is evident. While transition metal vacancies tend to structurally destabilize α-type compounds for all three systems, even at low alloy contents, a high amount of vacancies on the boron sublattice lead to a slight energetical stabilization at high amounts of silicon. Furthermore, only in $Ti(Si,B)_{2\pm z}$ the latter type of vacancies lead to a loss of AlB_2-type symmetry. These findings are in line with the prominent experimental discovery of highly defected metastable solid solutions in PVD thin films of ternary diborides.

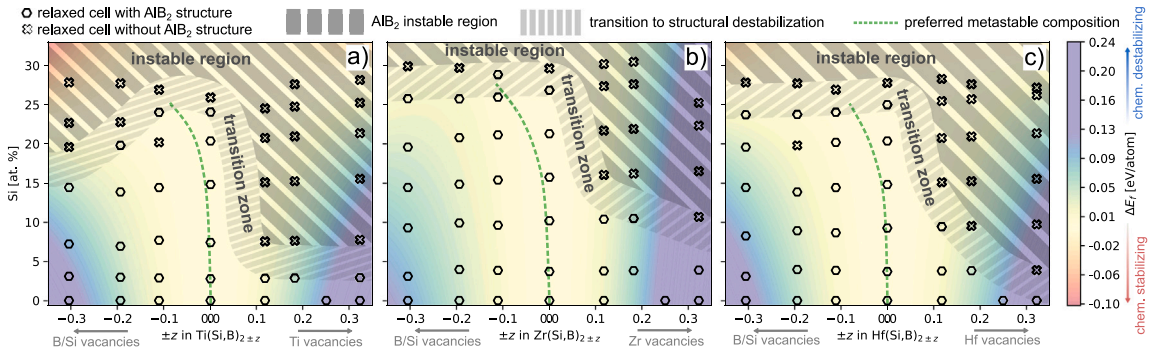

Fig. 9. Impact of boron and metal vacancies on the E_f of metastable (a) $Ti(Si,B)_{2\pm z}$, (b) $Zr(Si,B)_{2\pm z}$, and (c) $Hf(Si,B)_{2\pm z}$ compounds. On the horizontal axis the vacancy content z per formula unit is plotted, with positive values corresponding to vacancies on the metal sublattice, and negative values to boron sublattice vacancies. The vertical axis displays the Si content, while the color code of the contour plot corresponds to the influence of vacancies on the energies of formation of the regarded compound ΔE_f, as defined in the section of evaluation methods. Underlying data-points of the fitted contour plots are marked via hexagons, if the relaxed cell was of AlB_2 structure type, whereas crosses indicate results with highly distorted geometries. The illustrated green, dashed line acts as a guide for the reader, connecting compounds of preferred metastable composition, indicated through their lowest value of ΔE_f, in comparison to other compounds with the same alloy content. The gray, dashed area indicates supposed phase regions in composition space, containing compounds that are instable in a structure of the α-type. In accordance to the statistical observations made on the SQS cell distortion, a transition region is displayed between the AlB_2-stable and instable phase region.

4. Conclusions

First principle calculations were employed to study the structural and energetical properties of metastable Ti-Si-B_2, Zr-Si-B_2, and Hf-Si-B_2 revealing metastable solubility limits of 24 at. %, 27 at. %, and 25 at. %, respectively. A clear preference of Si to occupy the B sublattice was proven, as the lowest E_f was encountered for this alloying type. By employing a novel statistical approach, which considers multiple SQS cells of the same composition, a decaying structural integrity of the alloyed AlB_2-type structured supercells was encountered. This allowed to locate metastable solubility limits of Si, independent of the compound's non-equilibrium nature.

Comparing simulated XRD patterns with experimental thin film diffractograms resulted for both in an emerging loss in AlB_2-reflection intensities, with increasing Si content. Investigations of the RDFs revealed extensive clustering of silicon atoms, indicated by a shift of the mean Si-Si bond length from 2.1 Å to 2.4 Å. This clustering was found to be the main reason for the loss of the AlB_2-type symmetry above specific Si contents. An analysis of the chemical bonding in $TM(Si,B)_2$ compounds based on COHPs, revealed an incompatibility of mixed sp^2-sp^3 boron orbitals with Si-sp^3 states. The latter insight is represented by the anti-bonding nature of respective Si-Si and Si-B interactions, at elevated alloy contents. This leads to a weakened bond strength within the basal plane and substantial extension of the same, compared to minor alterations of the c lattice parameter. Simulations of the elastic properties revealed a decrease in Young's, bulk, and shear moduli, concerning an increasing amount of Si in $TM(Si,B)_2$. Indentation moduli of Ti-Si-$B_{2\pm z}$ and Hf-Si-$B_{2\pm z}$ based thin films were also found to compare well with the simulated data for contents up to 15 at. % Si. At the same time, a substantial increase in ductility was observed using Pugh and Pettifor's criteria. Regarding defected structures, metal vacancies clearly destabilize α-type structured TM-Si-B_2. Boron vacancies appeared compatible with AlB_2-type solid solutions and lead to no alteration of the chemical stability, at high alloy contents.

This study's findings on sublattice preferences, metastable Si solubility, and chemical bonding in ternary diborides enable the guided design of metastable quaternary and higher-order $TMB_{2\pm z}$-based systems, likely synthesizable via PVD methods.

CRediT authorship contribution statement

C. Gutschka: Writing – review & editing, Writing – original draft, Visualization, Investigation, Conceptualization. **L. Zauner:** Investigation. **T. Glechner:** Investigation. **D. Holec:** Writing – review & editing, Conceptualization. **H. Riedl:** Writing – review & editing, Supervision, Resources, Funding acquisition, Conceptualization.

Declaration of competing interest

The authors declare that they have no known competing financial interests or personal relationships that could have appeared to influence the work reported in this paper.

Acknowledgments

The financial support by the Austrian Federal Ministry for Digital and Economic Affairs, the National Foundation for Research, Technology and Development and the Christian Doppler Research Association is gratefully acknowledged (Christian Doppler Laboratory "Surface Engineering of high-performance Components"). We also thank for the financial support of Plansee SE, Plansee Composite Materials GmbH, and Oerlikon Balzers, Oerlikon Surface Solutions AG. The computational results presented have been achieved in part using the Vienna Scientific Cluster (VSC). The authors acknowledge TU Wien Bibliothek for financial support through its Open Access Funding Program.

Appendix A. Supplementary data

Supplementary material related to this article can be found online at https://doi.org/10.1016/j.actamat.2025.120857.

Data availability

The data that support the findings of this study are available from the corresponding author upon reasonable request.

References

[1] B.C. Wyatt, S.K. Nemani, G.E. Hilmas, E.J. Opila, B. Anasori, Ultra-high temperature ceramics for extreme environments, Nat. Rev. Mater. (2023) 1–17.
[2] G.-J. Zhang, D.-W. Ni, J. Zou, H.-T. Liu, W.-W. Wu, J.-X. Liu, T.S. Suzuki, Y. Sakka, Inherent anisotropy in transition metal diborides and microstructure/property tailoring in ultra-high temperature ceramics—A review, J. Eur. Ceram. Soc. 38 (2) (2018) 371–389.
[3] M. Magnuson, L. Hultman, H. Högberg, Review of transition-metal diboride thin films, Vacuum 196 (2022) 110567.
[4] R. Kiessling, A. Wetterholm, L.G. Sillén, A. Linnasalmi, P. Laukkanen, The crystal structures of molybdenum and tungsten borides, Acta Chem. Scand. 1 (10) (1947) 893–916.
[5] Y. Zhou, H. Xiang, Z. Feng, Z. Li, General trends in electronic structure, stability, chemical bonding and mechanical properties of ultrahigh temperature ceramics TMB2 (TM= transition metal), J. Mater. Sci. Technol. 31 (3) (2015) 285–294.

[6] F.R. Wagner, A.I. Baranov, Y. Grin, M. Kohout, A position-space view on chemical bonding in metal diborides with AlB2 type of crystal structure, Z. Für Anorg. Und Allg. Chem. 639 (11) (2013) 2025–2035.

[7] P. Vajeeston, P. Ravindran, C. Ravi, R. Asokamani, Electronic structure, bonding, and ground-state properties of AlB2-type transition-metal diborides, Phys. Rev. B 63 (4) (2001) 045115.

[8] P. Mayrhofer, C. Mitterer, J. Wen, J. Greene, I. Petrov, Self-organized nanocolumnar structure in superhard TiB_2 thin films, Appl. Phys. Lett. 86 (13) (2005).

[9] A. Goncharov, S. Dub, A. Agulov, V. Petukhov, Structure, composition, and mechanical properties of thin films of transition metals diborides, J. Superhard Mater. 37 (2015) 422–428.

[10] C. Mitterer, Borides in thin film technology, J. Solid State Chem. 133 (1) (1997) 279–291.

[11] C. Fuger, R. Hahn, A. Hirle, T. Wojcik, P. Kutrowatz, F. Bohrn, O. Hunold, P. Polcik, H. Riedl, Tissue phase affected fracture toughness of nano-columnar TiB_{2+z} thin films, Mater. Res. Lett. 11 (8) (2023) 613–622.

[12] J. Thörnberg, B. Bakhit, J. Palisaitis, N. Hellgren, L. Hultman, G. Greczynski, P.O. Persson, I. Petrov, J. Rosen, Improved oxidation properties from a reduced B content in sputter-deposited TiB_x thin films, Surf. Coat. Technol. 420 (2021) 127353.

[13] T. Glechner, O.E. Hudak, T. Wojcik, L. Haager, F. Bohrn, H. Hutter, O. Hunold, J. Ramm, S. Kolozsvári, E. Pitthan, et al., Influence of the non-metal species on the oxidation kinetics of Hf, HfN, HfC, and HfB_2 coatings, Mater. Des. 211 (2021) 110136.

[14] S. Dorri, J. Palisaitis, G. Greczynski, I. Petrov, J. Birch, L. Hultman, B. Bakhit, Oxidation kinetics of overstoichiometric TiB2 thin films grown by DC magnetron sputtering, Corros. Sci. 206 (2022) 110493.

[15] C. Fuger, B. Schwartz, T. Wojcik, V. Moraes, M. Weiss, A. Limbeck, C. Macauley, O. Hunold, P. Polcik, D. Primetzhofer, et al., Influence of Ta on the oxidation resistance of WB2 − z coatings, J. Alloys Compd. 864 (2021) 158121.

[16] W. Fahrenholtz, G. Hilmas, Oxidation of ultra-high temperature transition metal diboride ceramics, Int. Mater. Rev. 57 (1) (2012) 61–72.

[17] F. Monteverde, L. Scatteia, Resistance to thermal shock and to oxidation of metal diborides–SiC ceramics for aerospace application, J. Am. Ceram. Soc. 90 (4) (2007) 1130–1138.

[18] N. Nedfors, S. Mráz, J. Palisaitis, P.O. Persson, H. Lind, S. Kolozsvari, J.M. Schneider, J. Rosen, Influence of the Al concentration in Ti-Al-B coatings on microstructure and mechanical properties using combinatorial sputtering from a segmented TiB_2/AlB_2 target, Surf. Coat. Technol. 364 (2019) 89–98.

[19] T. Mościcki, R. Psiuk, J. Radziejewska, M. Wiśniewska, D. Garbiec, Properties of spark plasma sintered compacts and magnetron sputtered coatings made from Cr, Mo, Re and Zr alloyed tungsten diboride, Coatings 11 (11) (2021) 1378.

[20] B. Wicher, O. Pshyk, X. Li, B. Bakhit, V. Rogoz, I. Petrov, L. Hultman, G. Greczynski, Superhard oxidation-resistant $Ti_{1-x}Al_xB_y$ thin films grown by hybrid HiPIMS/DCMS co-sputtering diboride targets without external substrate heating, Mater. Des. 238 (2024) 112727.

[21] A. Kirnbauer, A. Wagner, V. Moraes, D. Primetzhofer, M. Hans, J. Schneider, P. Polcik, P. Mayrhofer, Thermal stability and mechanical properties of sputtered (Hf, Ta, V, W, Zr)-diborides, Acta Mater. 200 (2020) 559–569.

[22] P.H. Mayrhofer, A. Kirnbauer, P. Ertelthaler, C.M. Koller, High-entropy ceramic thin films; A case study on transition metal diborides, Scr. Mater. 149 (2018) 93–97.

[23] B. Bakhit, J. Palisaitis, Z. Wu, M.A. Sortica, D. Primetzhofer, P.O. Persson, J. Rosen, L. Hultman, I. Petrov, J.E. Greene, et al., Age hardening in superhard ZrB_2-rich $Zr_{1-x}Ta_xB_y$ thin films, Scr. Mater. 191 (2021) 120–125.

[24] Y. Li, C. Dong, X. Gu, J. Pan, R. Zhang, Z. Mu, M. Wen, K. Zhang, Exploring the potential for simultaneous enhancement of mechanical, wear and corrosion performance of the CrB_2 protective film actuated by soluting Si, Ceram. Int. 49 (22) (2023) 35082–35093.

[25] T. Fiantok, V. Šroba, N. Koutná, V. Izai, T. Roch, M. Truchlỳ, M. Vidiš, L. Satrapinskyy, v. Nagy, B. Grančič, et al., Structure evolution and mechanical properties of co-sputtered Zr-Al-B_2 thin films, J. Vac. Sci. Technol. A 40 (3) (2022).

[26] B. Bakhit, S. Dorri, A. Kooijman, Z. Wu, J. Lu, J. Rosen, J.M. Mol, L. Hultman, I. Petrov, J.E. Greene, et al., Multifunctional ZrB_2-rich $Zr_{1-x}Cr_xB_y$ thin films with enhanced mechanical, oxidation, and corrosion properties, Vacuum 185 (2021) 109990.

[27] R. Hahn, V. Moraes, A. Limbeck, P. Polcik, P.H. Mayrhofer, H. Euchner, Electron-configuration stabilized (W, Al)B_2 solid solutions, Acta Mater. 174 (2019) 398–405.

[28] A.H.N. Kashani, S. Mráz, D.M. Holzapfel, M. Hans, L. Löfler, P. Ondračka, D. Primetzhofer, J.M. Schneider, Synthesis and oxidation behavior of $Ti_{0.35}Al_{0.65}B_y$ (y= 1.7-2.4) coatings, Surf. Coat. Technol. 442 (2022) 128190.

[29] B. Bakhit, J. Palisaitis, J. Thörnberg, J. Rosen, P.O. Persson, L. Hultman, I. Petrov, J.E. Greene, G. Greczynski, Improving the high-temperature oxidation resistance of TiB2 thin films by alloying with Al, Acta Mater. 196 (2020) 677–689.

[30] A. Bahr, T. Glechner, A. Grimmer, T. Wojcik, R. Hahn, P. Kutrowatz, M. Podsednik, A. Limbeck, M. Heller, J. Ramm, et al., High-temperature oxidation resistance of ternary and quaternary Cr-(Mo)-Si-B_{2-z} coatings—Influence of Mo addition, Surf. Coat. Technol. 468 (2023) 129733.

[31] A. Bahr, O. Beck, T. Glechner, A. Grimmer, T. Wojcik, P. Kutrowatz, J. Ramm, O. Hunold, S. Kolozsvári, P. Polcik, et al., Quaternary diborides—improving the oxidation resistance of $TiB_{2\pm z}$ coatings by disilicide alloying, Mater. Res. Lett. 11 (9) (2023) 733–741.

[32] P. Spencer, Thermodynamic prediction of metastable coating structures in PVD processes, Int. J. Mater. Res. 92 (10) (2022) 1145–1150.

[33] H. Holleck, Metastable coatings—Prediction of composition and structure, Surf. Coat. Technol. 36 (1–2) (1988) 151–159.

[34] H. Holleck, Advanced concepts of PVD hard coatings, Vacuum 41 (7–9) (1990) 2220–2222.

[35] F.H. Löffler, Formation of non-equilibrium phases in the PVD process, Vacuum 43 (5–7) (1992) 397–402.

[36] F. Kiryukhantsev-Korneev, M. Lemesheva, N. Shvyndina, E. Levashov, A.Y. Potanin, Structure, mechanical properties, and oxidation resistance of ZrB_2, ZrSiB, and ZrSiB/SiBC coatings, Prot. Met. Phys. Chem. Surfaces 54 (2018) 1147–1156.

[37] B. Grančič, M. Mikula, T. Roch, P. Zeman, L. Satrapinskyy, M. Gregor, T. Plecenik, E. Dobročka, Z. Hájovská, M. Mičušík, et al., Effect of Si addition on mechanical properties and high temperature oxidation resistance of Ti-B-Si hard coatings, Surf. Coat. Technol. 240 (2014) 48–54.

[38] T. Glechner, R. Hahn, A. Bahr, T. Wojcik, M. Weiss, J. Ramm, O. Hunold, P. Polcik, H. Riedl, Oxidation resistance of Si doped transition metal diborides at elevated temperatures, Int. J. Refract. Met. Hard Mater. 113 (2023) 106172.

[39] L. Zauner, R. Hahn, O. Hunold, J. Ramm, S. Kolozsvári, P. Polcik, H. Riedl, Influence of Si segregates on the structural evolution, mechanical properties, and high-temperature fracture toughness of Cr-Si-$B_{2\pm z}$ coatings, J. Alloys Compd. 958 (2023) 170354.

[40] L. Zauner, A. Steiner, T. Glechner, A. Bahr, B. Ott, R. Hahn, T. Wojcik, O. Hunold, J. Ramm, S. Kolozsvári, et al., Role of Si segregation in the structural, mechanical, and compositional evolution of high-temperature oxidation resistant Cr-Si-$B_{2\pm z}$ thin films, J. Alloys Compd. 944 (2023) 169203.

[41] T. Glechner, H. Oemer, T. Wojcik, M. Weiss, A. Limbeck, J. Ramm, P. Polcik, H. Riedl, Influence of Si on the oxidation behavior of TM-Si-$B_{2\pm z}$ coatings (TM=Ti, Cr, Hf, Ta, W), Surf. Coat. Technol. 434 (2022) 128178.

[42] T. Glechner, A. Bahr, R. Hahn, T. Wojcik, M. Heller, A. Kirnbauer, J. Ramm, S. Kolozsvari, P. Felfer, H. Riedl, High temperature oxidation resistance of physical vapor deposited Hf-Si-$B_{2\pm z}$ thin films, Corros. Sci. 205 (2022) 110413.

[43] N. Hamdad, N. Benosman, B. Bouhafs, First principles calculation of electronic structure, bonding and chemical stability of TiB2, NbB2 and their ternary alloy Ti0. 5Nb0. 5B2, Phys. B 405 (2) (2010) 540–546.

[44] Q. Xie, Y. Yao, X. Liu, J. Sun, Z. Zhang, L. Chen, Theoretical study on mechanical and electronic properties of ternary diborides Sc0. 5V0. 5B2, Sc0. 5Nb0. 5B2 and Sc0. 5Ta0. 5B2, Mater. Today Commun. 35 (2023) 105760.

[45] W. Qi, B. Chen, X. Yang, N. Liu, Z. Jia, W. Wang, Phase stability, mechanical and thermodynamic properties of (Hf, Zr, Ta, M) B2 (M=Nb, Ti, Cr, W) quaternary high-entropy diboride ceramics via first-principles calculations, Ceram. Int. 49 (20) (2023) 33255–33264.

[46] S.-Y. Liu, L. Qin, H. Zhang, C. Liu, S. Liu, D.-J. Li, T. Yadav, D. Shah, S. Wang, Design of superhard high-entropy diborides via high-throughput DFT and thermodynamics calculations, Ceram. Int. (2024).

[47] V. Moraes, H. Riedl, C. Fuger, P. Polcik, H. Bolvardi, D. Holec, P.H. Mayrhofer, Ab initio inspired design of ternary boride thin films, Sci. Rep. 8 (1) (2018) 9288.

[48] W.A. Zdaniewski, Solid solubility effect on properties of titanium diboride, J. Am. Ceram. Soc. 70 (11) (1987) 793–797.

[49] E.W. Neuman, G.E. Hilmas, W.G. Fahrenholtz, Transition metal diboride-silicon carbide-boron carbide ceramics with super-high hardness and strength, J. Eur. Ceram. Soc. 42 (15) (2022) 6795–6801.

[50] L. Feng, W.G. Fahrenholtz, D.W. Brenner, High-entropy ultra-high-temperature borides and carbides: a new class of materials for extreme environments, Annu. Rev. Mater. Res. 51 (1) (2021) 165–185.

[51] C. Schmalzried, R. Telle, B. Freitag, W. Mader, Solid state reactions in transition metal diboride-based materials, Int. J. Mater. Res. 92 (11) (2022) 1197–1202.

[52] S. Vorotilo, E. Levashov, V. Kurbatkina, E. Patsera, P. Loginov, V.Y. Lopatin, A. Orekhov, Theoretical and experimental study of combustion synthesis of microgradient ULTRA high-temperature ceramics in Zr-Ta-Si-B system, J. Eur. Ceram. Soc. 41 (9) (2021) 4728–4746.

[53] H. Euchner, P.H. Mayrhofer, Designing thin film materials—Ternary borides from first principles, Thin Solid Films 583 (2015) 46–49.

[54] B. Alling, H. Högberg, R. Armiento, J. Rosén, L. Hultman, A theoretical investigation of mixing thermodynamics, age-hardening potential and electronic structure of ternary $M^1{}_{1-x}M^2{}_xB_2$ alloys with AlB_2 type structure, Sci. Rep. 5 (1) (2015) 9888.

[55] A.S. Ramos, R. Baldan, C.A. Nunes, G.C. Coelho, P.A. Suzuki, G. Rodrigues, Isothermal section of the Ti-Si-B system at 1250° C in the Ti-TiSi2-TiB2 region, Mater. Res. 17 (2014) 392–396.

[56] Y. Yang, Y. Chang, L. Tan, Thermodynamic modeling and experimental investigation of the Ti-rich corner of the Ti–Si–B system, Intermetallics 13 (10) (2005) 1110–1115.
[57] F. Han, Y. Zhan, H. Luo, Phase equilibria in the Zr-Si-B ternary system (Zr-Si-ZrB_2 region) at 1173 K, Int. J. Mater. Res. 108 (10) (2017) 808–814.
[58] L.A. Borges Junior, A.A.A. Pinto da Silva, G.C. Coelho, C.A. Nunes, Liquidus projection of the Zr-Si-B ternary system, J. Phase Equilibria Diffus. 41 (2020) 123–131.
[59] R. Sakidja, J. Myers, S. Kim, J. Perepezko, The effect of refractory metal substitution on the stability of Mo (ss)+ T2 two-phase field in the Mo–Si–B system, Int. J. Refract. Met. Hard Mater. 18 (4–5) (2000) 193–204.
[60] S. Katrych, A. Grytsiv, A. Bondar, P. Rogl, T. Velikanova, M. Bohn, Structural materials: metal–silicon–boron: on the melting behavior of Mo–Si–B alloys, J. Alloys Compd. 347 (1–2) (2002) 94–100.
[61] A.A.A.P. da Silva, N. Chaia, F. Ferreira, G.C. Coelho, J.-M. Fiorani, N. David, M. Vilasi, C.A. Nunes, Thermodynamic modeling of the V-Si-B system, Calphad 59 (2017) 199–206.
[62] M. Yazlak, H.-J. Christ, W. Yang, G. Hasemann, M. Krüger, B. Gorr, Thermodynamic modelling of the V–Ti–B system, Calphad 79 (2022) 102477.
[63] G. Cai, F. Zheng, D. Yi, H. Chen, S. Zhou, Z. Long, Z. Jin, Experimental investigation and thermodynamic modeling of Hf–Si–B system, J. Alloys Compd. 494 (1–2) (2010) 148–154.
[64] V. Behrani, A.J. Thom, M.J. Kramer, M. Akinc, Microstructure and oxidation behavior of Nb–Mo–Si–B alloys, Intermetallics 14 (1) (2006) 24–32.
[65] Z. Sun, Y. Yang, X. Guo, C. Zhang, Y.A. Chang, Thermodynamic modeling of the Nb-rich corner in the Nb–Si–B system, Intermetallics 19 (1) (2011) 26–34.
[66] C.E. Campbell, U.R. Kattner, Assessment of the Cr-B system and extrapolation to the Ni-Al-Cr-B quaternary system, Calphad 26 (3) (2002) 477–490.
[67] T.T. Dorini, B.X. de Freitas, P.P. Ferreira, N. Chaia, P.A. Suzuki, J.-M. Joubert, C.A. Nunes, G.C. Coelho, L.T. Eleno, T2 phase site occupancies in the Cr–Si–B system: a combined synchroton-XRD/first-principles study, Scr. Mater. 199 (2021) 113854.
[68] V. Chad, N. Chaia, T. Villela, C. Nunes, G. Coelho, Experimental determination of liquidus projection in the Cr rich region of the Cr-Si-B system, J. Alloys Compd. 772 (2019) 735–739.
[69] Y. Yang, Y. Chang, L. Tan, W. Cao, Multiphase equilibria in the metal-rich region of the Mo–Ti–Si–B system: thermodynamic prediction and experimental validation, Acta Mater. 53 (6) (2005) 1711–1720.
[70] M. Zhao, W. Ye, M. Zhu, Y. Gui, W. Guo, S. Wu, Y. Yan, From Mo-Si-B to Mo-Ti-Si-B alloys: A short review, Materials 16 (1) (2022) 3.
[71] M.E. Schlesinger, Thermodynamics of solid transition-metal silicides, Chem. Rev. 90 (4) (1990) 607–628.
[72] X. Chen, C. Liang, Transition metal silicides: fundamentals, preparation and catalytic applications, Catal. Sci. Technol. 9 (18) (2019) 4785–4820.
[73] M. Dahlqvist, J. Rosen, Impact of vacancies on structure, stability and properties of hexagonal transition metal diborides, MB_2 (M=Sc, Y, Ti, Zr, Hf, V, Nb, Ta, Cr, Mo, W, Mn, and Fe), Materialia 26 (2022) 101629.
[74] S.-Y. Liu, C. Liu, S. Zhang, S. Liu, D.-J. Li, Y. Li, S. Wang, Phase diagram and mechanical properties of fifteen quaternary high-entropy metal diborides: First-principles calculations and thermodynamics, J. Appl. Phys. 131 (7) (2022).
[75] M. Dahlqvist, Q. Tao, J. Zhou, J. Palisaitis, P.O. Persson, J. Rosen, Theoretical prediction and synthesis of a family of atomic laminate metal borides with in-plane chemical ordering, J. Am. Chem. Soc. 142 (43) (2020) 18583–18591.
[76] A. Zunger, S.-H. Wei, L. Ferreira, J.E. Bernard, Special quasirandom structures, Phys. Rev. Lett. 65 (3) (1990) 353.
[77] D. Gehringer, M. Friák, D. Holec, Models of configurationally-complex alloys made simple, Comput. Phys. Comm. 286 (2023) 108664.
[78] G. Kresse, J. Furthmüller, Efficient iterative schemes for ab initio total-energy calculations using a plane-wave basis set, Phys. Rev. B 54 (16) (1996) 11169.
[79] G. Kresse, D. Joubert, From ultrasoft pseudopotentials to the projector augmented-wave method, Phys. Rev. B 59 (3) (1999) 1758.
[80] P.E. Blöchl, Projector augmented-wave method, Phys. Rev. B 50 (24) (1994) 17953.
[81] Available PAW potentials, 2024, https://www.vasp.at/wiki/index.php/Available_PAW_potentials (Accessed: 2024-21-04).
[82] J.P. Perdew, K. Burke, M. Ernzerhof, Generalized gradient approximation made simple, Phys. Rev. Lett. 77 (18) (1996) 3865.
[83] M. Methfessel, A. Paxton, High-precision sampling for Brillouin-zone integration in metals, Phys. Rev. B 40 (6) (1989) 3616.
[84] T. Bučko, J. Hafner, J.G. Ángyán, Geometry optimization of periodic systems using internal coordinates, J. Chem. Phys. 122 (12) (2005).
[85] T. Glechner, R. Hahn, L. Zauner, S. Rißlegger, A. Kirnbauer, P. Polcik, H. Riedl, Structure and mechanical properties of reactive and non-reactive sputter deposited WC based coatings, J. Alloys Compd. 885 (2021) 161129.
[86] G. Pharr, W. Oliver, Measurement of thin film mechanical properties using nanoindentation, Mrs Bull. 17 (7) (1992) 28–33.
[87] W.C. Oliver, G.M. Pharr, An improved technique for determining hardness and elastic modulus using load and displacement sensing indentation experiments, J. Mater. Res. 7 (6) (1992) 1564–1583.
[88] K. Momma, F. Izumi, VESTA: a three-dimensional visualization system for electronic and structural analysis, J. Appl. Crystallogr. 41 (3) (2008) 653–658.
[89] S.P. Ong, W.D. Richards, A. Jain, G. Hautier, M. Kocher, S. Cholia, D. Gunter, V.L. Chevrier, K.A. Persson, G. Ceder, Python Materials Genomics (pymatgen): A robust, open-source python library for materials analysis, Comput. Mater. Sci. 68 (2013) 314–319.
[90] S. Menon, G.D. Leines, J. Rogal, pyscal: A python module for structural analysis of atomic environments, J. Open Source Softw. 4 (43) (2019) 1824.
[91] R. Dronskowski, P.E. Bloechl, Crystal orbital Hamilton populations (COHP): energy-resolved visualization of chemical bonding in solids based on density-functional calculations, J. Phys. Chem. 97 (33) (1993) 8617–8624.
[92] V.L. Deringer, A.L. Tchougréeff, R. Dronskowski, Crystal orbital Hamilton population (COHP) analysis as projected from plane-wave basis sets, J. Phys. Chem. A 115 (21) (2011) 5461–5466.
[93] S. Maintz, V.L. Deringer, A.L. Tchougréeff, R. Dronskowski, Analytic projection from plane-wave and PAW wavefunctions and application to chemical-bonding analysis in solids, J. Comput. Chem. 34 (29) (2013) 2557–2567.
[94] S. Maintz, V.L. Deringer, A.L. Tchougréeff, R. Dronskowski, LOBSTER: A Tool to Extract Chemical Bonding from Plane-Wave based DFT, Wiley Online Library, 2016.
[95] R. Yu, J. Zhu, H. Ye, Calculations of single-crystal elastic constants made simple, Comput. Phys. Comm. 181 (3) (2010) 671–675.
[96] M. Moakher, A.N. Norris, The closest elastic tensor of arbitrary symmetry to an elasticity tensor of lower symmetry, J. Elasticity 85 (2006) 215–263.
[97] A. Reuss, Computation of the yield point of mixed crystals due to hiring for single crystals, Math. Phys. 9 (1929) 49–58.
[98] F. Povolo, R. Bolmaro, Average elastic constants and tensor invariants, Phys. Status Solidi (A) 99 (2) (1987) 423–436.
[99] N. Abdoshahi, M. Dehghani, L. Hatzenbichler, P. Spoerk-Erdely, A.V. Ruban, M. Musi, S. Mayer, J. Spitaler, D. Holec, Structural stability and mechanical properties of TiAl+Mo alloys: A comprehensive ab initio study, Acta Mater. 221 (2021) 117427.
[100] S. Pugh, XCII. Relations between the elastic moduli and the plastic properties of polycrystalline pure metals, Lond. Edinb. Dublin Philos. Mag. J. Sci. 45 (367) (1954) 823–843.
[101] D. Pettifor, Theoretical predictions of structure and related properties of intermetallics, Mater. Sci. Technol. 8 (4) (1992) 345–349.
[102] W. Sun, S.T. Dacek, S.P. Ong, G. Hautier, A. Jain, W.D. Richards, A.C. Gamst, K.A. Persson, G. Ceder, The thermodynamic scale of inorganic crystalline metastability, Sci. Adv. 2 (11) (2016) e1600225.
[103] A. Jain, S.P. Ong, G. Hautier, W. Chen, W.D. Richards, S. Dacek, S. Cholia, D. Gunter, D. Skinner, G. Ceder, et al., Commentary: The Materials Project: A materials genome approach to accelerating materials innovation, APL Mater. 1 (1) (2013).
[104] J.W. Arblaster, Selected Values of the Crystallographic Properties of the Elements, ASM International, 2018.
[105] G. Abadias, M. Kanoun, S. Goumri-Said, L. Koutsokeras, S. Dub, P. Djemia, Electronic structure and mechanical properties of ternary ZrTaN alloys studied by ab initio calculations and thin-film growth experiments, Phys. Rev. B 90 (14) (2014) 144107.
[106] G. Abadias, V. Ivashchenko, L. Belliard, P. Djemia, Structure, phase stability and elastic properties in the $Ti_{1-x}Zr_xN$ thin-film system: Experimental and computational studies, Acta Mater. 60 (15) (2012) 5601–5614.
[107] S. Aouadi, Structural and mechanical properties of TaZrN films: Experimental and ab initio studies, J. Appl. Phys. 99 (5) (2006).
[108] A. Ivanovskii, Hardness of hexagonal AlB_2-like diborides of s, p and d metals from semi-empirical estimations, Int. J. Refract. Met. Hard Mater. 36 (2013) 179–182.
[109] M. Audronis, A. Leyland, A. Matthews, J. Wen, I. Petrov, Characterization studies of pulse magnetron sputtered hard ceramic titanium diboride coatings alloyed with silicon, Acta Mater. 56 (16) (2008) 4172–4182.
[110] R. Thompson, W. Clegg, Predicting whether a material is ductile or brittle, Curr. Opin. Solid State Mater. Sci. 22 (3) (2018) 100–108.
[111] T. Glechner, R. Hahn, T. Wojcik, D. Holec, S. Kolozsvári, H. Zaid, S. Kodambaka, P.H. Mayrhofer, H. Riedl, Assessment of ductile character in superhard Ta-CN thin films, Acta Mater. 179 (2019) 17–25.
[112] D.G. Sangiovanni, V. Chirita, L. Hultman, Electronic mechanism for toughness enhancement in Ti_x M_{1-x} N (M=Mo and W), Phys. Rev. B 81 (10) (2010) 104107.
[113] R. Andrievski, G. Kalinnikov, J. Jauberteau, J. Bates, Some peculiarities of fracture of nanocrystalline nitride and boride films, J. Mater. Sci. 35 (2000) 2799–2806.